Journal of Quantitative Spectroscopy & Radiative Transfer 000 (2020) 106730

Contents lists available at ScienceDirect

Journal of Quantitative Spectroscopy & Radiative Transfer

journal homepage: www.elsevier.com/locate/jqsrt

A closure study of ocean inherent optical properties using flow cytometry measurements

Yangyang Zhao[a,e,*], Carina Poulin[b], David McKee[c], Lianbo Hu[a,f], Jacopo Agagliate[c,g], Ping Yang[d], Zhang Xiaodong[a]

[a] Department of Earth System Science and Policy, University of North Dakota, 4149 University Ave Stop 9011, Grand Forks, ND 58202, USA
[b] Department of Marine Science, The University of Southern Mississippi, 1020 Balch Boulevard, Stennis Space Center, MS 39529, USA
[c] Department of Physics of the University of Strathclyde, 107 Rottenrow East, Glasgow G4 0NG, UK
[d] Department of Atmospheric Sciences, Texas A&M University, TAMU-3150, College Station, Texas 77843, USA
[e] Building 14, Apt. 3-402, Xianggang dong road No.23, Qingdao, Shandong 266071, China
[f] Ocean Remote Sensing Institute, Ocean University of China, Qingdao, 266003, China
[g] Institute of Coastal Research of the Helmholtz-Zentrum Geesthacht, Max-Planck-Str. 1, Building 70, Geesthacht, DE D-21502, Germany

ARTICLE INFO

Article history:
Received 29 August 2019
Revised 25 October 2019
Accepted 26 October 2019
Available online xxx

Keywords:
Optical closure
Size
Refractive index
Shape
Structure
Models

ABSTRACT

Flow cytometry and inherent optical property measurements of UK coastal waters were used to evaluate optical closure of different combinations of models for particle size, refractive index and shape. The particle size and refractive index distributions were derived from flow cytometry measurements and subsequently simplified through averaging down to the simplest model consisting of a Junge size distribution with a single bulk refractive index. Models for particle shapes included homogeneous spheres, coated spheres, and hexahedra. The simplest particle model, based on a Junge size distribution and a single bulk refractive index, gave the poorest quality of closure, suggesting that it underestimates particle complexity in the sampled waters. Other particle models using more detailed combinations of size and refractive index distributions gave broadly equivalent results for absorption and scattering. Backscattering was better represented by the most complex particle size and refractive index model, indicating that backscattering is sensitive to those factors. The homogeneous spherical model gave relatively good results, which is expected because the inversion of size and refractive index distributions from flow cytometry is based on the homogeneous spherical model using forward and side scattering signals. Lorenz-Mie theory, assuming homogeneous spheres, provided optical closure that was generally as accurate as models with more complex particle shape and structure. Cumulative contribution simulations revealed that particles between 0.5 and 20 μm substantially contributed to attenuation, scattering and backscattering, while particles larger than 20 μm mainly contributed to absorption and small particles (< 0.5 μm) contribute to 30–40% of backscattering.

1. Introduction

The characteristics of particle assemblages in water deter mine their optical properties [16]. Closure studies comparing simulated optical properties based on particle characterization with observed optical properties are critical for improving the current level of knowledge of the roles played by various particle species and for developing physically based inversion models characterizing particles from optical observations [7,8,16,18,20,26,29,33].

Ackleson and Spinrad [2] pioneered a flow cytometry (FC) approach to extract both the size and refractive index of particles from measurements of forward scattering (1.5–19°) and side scattering (73–107°) using the Lorenz-Mie theory, which assumes particles to be homogeneous spheres. Green et al. [14] improved the method by adding measurements of chlorophyll fluorescence to determine the sizes and complex refractive indices of marine particles. The Ackleson-Green inversion approach has recently been applied to the retrievals of particle backscattering cross sections [12,23].

* Corresponding author.
E-mail addresses: yangyang.zhao91@outlook.com (Y. Zhao), carina.poulin@usm.edu (C. Poulin), david.mckee@strath.ac.uk (D. McKee), lianbo.hu@und.edu (L. Hu), Jacopo.Agagliate@hzg.de (J. Agagliate), pyang@tamu.edu (P. Yang), Xiaodong.Zhang@usm.edu (Z. Xiaodong).

https://doi.org/10.1016/j.jqsrt.2019.106730

Concurrent measurements of FC and inherent optical properties (IOPs) allow optical closure to be examined. Such a study was recently conducted by Agagliate et al. [4] with FC and measurements of the absorption coefficient, the attenuation coefficient, and the volume scattering function (VSF, β) at 124° for UK coastal waters. FC-derived particle size distributions over a size range of 0.5–20 μm were extrapolated to the optically-significant size range of 0.05–2000 μm [11]. Using models with FC-derived refractive indices and extrapolated particle size distributions (PSDs) as inputs and assuming particles to be homogeneous spheres, retrievals were in agreement with in situ IOP measurements, with root mean square percentage error (RMS%E) = 35% for scattering, 45% for backscattering, and 77% for backscattering ratio, but poor agreement (RMS%E = 202%) for absorption, which was attributed to a lack of information about the imaginary part of the refractive index provided by FC [4].

However, with the exception of bubbles, natural oceanic particles are neither spherical nor homogeneous [37]. Clavano et al. [9] simulated the bulk IOPs of attenuation, absorption and scattering coefficients for polydisperse spheroids and spheres of equivalent volumes and found that the spherical assumption generally underestimates these bulk IOPs, with deviations up to a factor of two with increasing proportions of large particles. This is mainly because the scattering and absorption (and hence the total attenuation) coefficients of large particles are proportional to the cross-sectional areas of particles, and a sphere has the smallest cross-section compared to other convex shapes of equal volume. It is well known that a homogeneous spherical model underestimates the backscattering of phytoplankton cells that are morphologically heterogeneous [19,22,28]. Poulin et al. [27] showed that the use of coated spheres can well represent the diel variation of the VSFs at 124° measured for four phytoplankton species grown in cultures. Similarly, Organelli et al. [24] showed that both attenuation and backscattering coefficients measured in situ for particles can be reproduced using coated spheres.

In this study, we reexamine the closure study by Agagliate et al. [4] with a focus on the effects of particle shape and structure instead of assuming homogeneous spherical particles. In particular, we use non-symmetrical hexahedra with acute edges, representing a diametric extreme of a sphere to examine the effect of particle shape. We also use coated spheres to examine the effect of inhomogeneous particle structure. This study provides insight about the applicability of the Lorenz-Mie model to simulations of IOPs and the extent to which IOP simulations can be further improved by assuming that oceanic particles are non-spherical and/or inhomogenous.

2. Data and methods

2.1. UK coastal water dataset

The data used for this study were also used in Agagliate et al. [[3] and [4]]. Briefly, the inherent optical properties, namely particulate attenuation (c_p; m^{-1}) and absorption (a_p; m^{-1}) coefficients, and the VSF at 124° $\beta(124^o)$ were measured at 62 stations from April 4–21, 2015 on board the RV Heincke in coastal waters around the UK (see Fig. 1 in [4]). A total of 50 collocated water samples were collected for FC analysis to derive the particle size distribution (PSD) and particle refractive index distributions (PRIDs).

2.2. Measurements of IOPs

The VSFs were measured using a Sea-Bird/WET Labs BB-9 sensor with a centroid scattering angle of 124° The VSF measurements were corrected for attenuation along the path length. The contribution by pure seawater was calculated using Zhang et al. [36] with concurrently measured inputs of temperature and salinity and was subsequently subtracted from attenuation-corrected VSF measurements. To estimate the particulate backscattering ratio, a value of 0.9 for the χ factor was used following Lefering et al. [20]. Absorption and attenuation coefficients were measured using a Sea-Bird/WET Labs ac-9 instrument. Salinity-temperature dependence correction for ac-9 measurements was applied following Pegau et al. [25]. The scattering loss of ac-9 measurement comes from two sources: The absorption sensor is unable to capture scattered light at angles greater than 41° and the attenuation sensor collects all photons scattered in forward directions within an acceptance angle of 0.9°. McKee et al. [21] developed an iterative correction for both absorption and attenuation measurements. This iterative correction requires knowledge of the particulate phase function, which can be approximated in terms of the Fournier and Forand [13] analytical formula with a backscattering ratio calculated using the backscattering coefficient (b_{bp}, m^{-1}) from BB-9 measurements and b_p from ac-9 measurements. In addition, the attenuation correction for BB-9 measurements requires c_p measured by the ac-9. These iterative ac-9 and BB-9 corrections are illustrated schematically in Fig. 1. The closure analysis was carried out at 532 nm, at which wavelength both the ac-9 and the BB-9 take measurements.

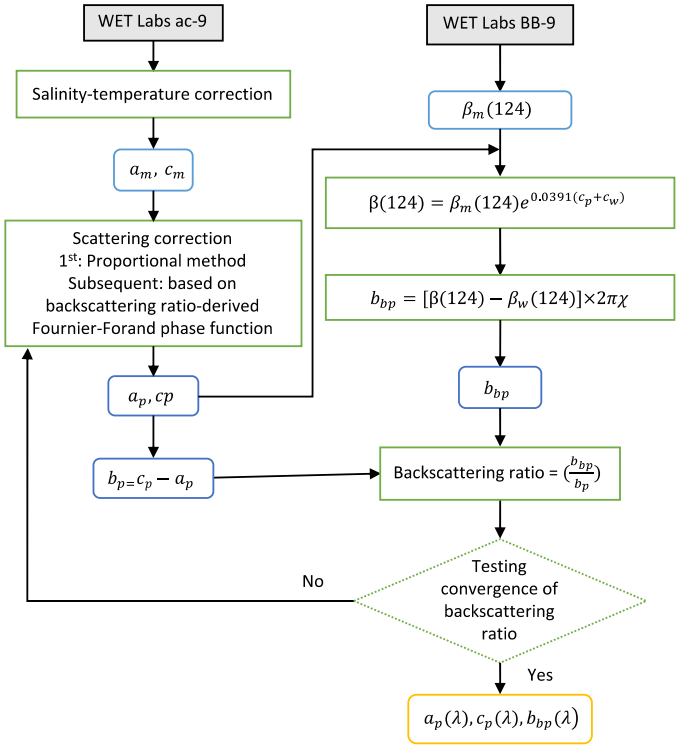

Fig. 1. Schematic illustration of the iterative procedure correcting for the scattering loss in the ac-9 measurements of particulate absorption (a_p) and particulate attenuation (c_p) coefficients and correcting for the attenuation loss in the BB-9 measurements of the volume scattering function at a scattering angle of 124° ($\beta(124)$).

2.3. Flow cytometry measurement and PSD models

Water samples were analyzed using a CytoSense flow cytometer (CytoBuoy b.v., The Netherlands) equipped with a 488 nm laser following Ackleson and Spinrad [2] and Green et al. [14] to retrieve particle sizes and refractive indices. The retrievals of particle diameter (D) and the real part of the refractive indices (n_r) were conducted in conjunction with lookup tables calculated using the Lorenz-Mie theory at scattering angles of 1.5–19° (forward) and of 73–107° (side) [3]. For the imaginary part of the refrac-

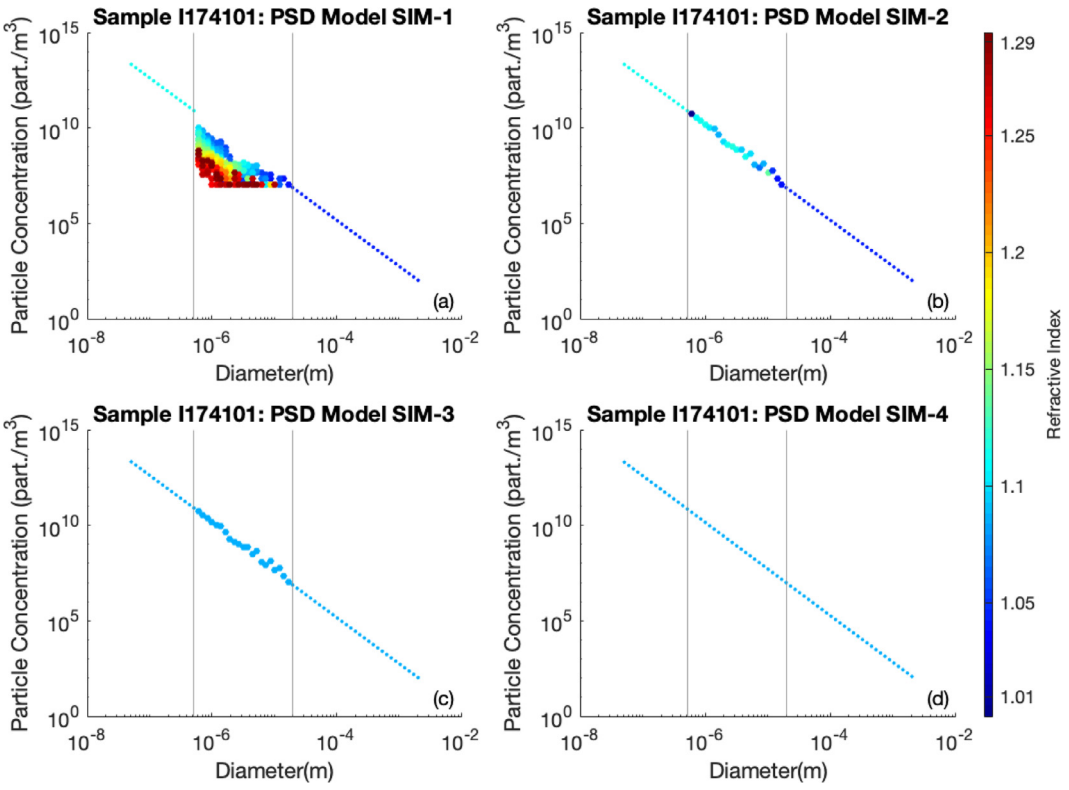

Fig. 2. a) An example of particle size distribution (PSD; m^{-3} µm^{-1}) and refractive index distribution (dots of different colors) derived from FC as a function of central particle diameter (D) of each size bin. b) Total particle size distribution and mean n_r in each size bin. c) Same as b for total particle size distribution but with a global mean n_r averaged for all size bins. d) The Junge (power-law) [17] distribution fitted to the PSD in c with a global mean n_r over all size bins. The dotted lines in a-d are the extrapolation of the fitted Junge distribution delimited by the gray lines in a-c and in d down to 0.05 µm and up to 2000 µm, respectively, to cover the optically significant size range of particles (see text for details). The colors of the dots correspond to the real part of the refractive indexes (n_r) (For interpretation of the references to color in this figure legend, the reader is referred to the web version of this article.).

tive index (n_i), we used the values reported in Babin et al. [5]. At 532 nm, $n_i = 0.0009$ for $n_r \geq 1.1$ (roughly representing mineral particles) and $n_i = 0.001$ for $n_r < 1.1$ (roughly representing organic/phytoplankton particles). This was used for every model except the coated spherical model, for which we used $n_i = 0.0015$ for the core for all wavelengths following Poulin et al. [27] who used $n_i = 0.0015$ for *D. tertiolecta* at 651 nm with coated spherical models. The complex refractive index of particles is then represented as $n = n_r + in_i$.

An example of FC-derived particle concentration and index distributions at each size bin are shown in Fig. 2a as colored dots, where different colors denote different values of n_r. From this original FC product, we applied three levels of progressive averaging to simplify the size and/or refractive index distributions. First, we calculated the total particle size distribution (PSD) and concentration-weighted average refractive index ($n_b = n_{r,b} + in_{i,b}$) for each size bin. The results are shown as colored dots in Fig. 2b, where different colors correspond to values of $n_{r,b}$. We further averaged the refractive indices shown in Fig. 2b to calculate a global average index n_g ($n_g = n_{r,g} + in_{i,g}$). The results are shown as dots in Fig. 2c, where the color of dots denotes the value of $n_{r,g}$. Finally, we fitted Junge's (power-law) distribution to the data points shown in Fig. 2c:

$$PSD(D) = kD^{-\gamma} \quad (1)$$

where PSD represents particle size distribution in units of m^{-3} µm^{-1}, and γ denotes the exponent or the slope and k is the scaling factor related to the total particle concentration within the FC size range. The dotted line in Fig. 2d represents the fitted Junge size distribution with a global mean refractive index of n_g. The values of γ for all samples ranged from 2.86 – 3.64 with a mean of 3.36.

While the FC method is primarily sensitive to particles of a size range between approximately 0.5 µm to 20 µm, particles of all sizes contribute to the bulk IOPs measured in the field. To reconcile this difference, we extrapolated the fitted Junge distribution to an extended size range of 0.05 – 2000 µm [11]. In extrapolation, we ensured the continuity of the concentration and the refractive index of particles at the two end size bins (as illustrated in Fig. 2b). For example, at the lower end of the size bins ($D = 0.5$ µm), we modified the value of k (Eq. (1)) so $kD^{-\gamma}$ at $D = 0.5$ µm is equal to the total particle concentration per bin width estimated from FC at 0.5 µm. Moreover, we assumed the refractive index for the extrapolated distribution is the same as the refractive index estimated for the smallest measured bin ($D = 0.5$ µm). The same procedure was applied for the extrapolation at the upper end of the size bins ($D = 20$ µm). Particle distributions as those derived in Fig. 2b typically have different refractive indices for the lower and upper ends of the size bins, so the extrapolated distributions also have different refractive indices between the lower and upper extrapolations. To apply the extrapolation to the original FC data as shown in Fig. 2a, for which particles in each size bin could have different refractive indices, we simply duplicated the extrapolation developed in Fig. 2b. The extrapolations are shown in Fig. 2 as dotted lines. The particle distributions derived in Fig. 2c and d have one global mean refractive index; as a result, the extrapolated distributions also have only one refractive index.

All four PSD and refractive index models shown in Fig. 2 were used for further analysis. We refer to these four models as SIM-1 (Size and Index Model-1), SIM-2, SIM-3, and SIM-4. These four models differ in the details on how the particle refractive index (a proxy for particle composition) and concentration are represented.

The most detailed information on particles as provided by the FC measurements is preserved in SIM-1 (Fig. 2a), where particles of different refractive index in each size bin are counted separately. Both SIM-2 (Fig. 2b) and SIM-3 (Fig. 2c) represent particles within each size bin with a bin-total concentration, but differ in how the refractive index is represented. SIM-2 assigns particles in each size bin a bin-average index, whereas SIM-3 assigns particles in all bins a global average index. SIM-4 (Fig. 2d) is an idealized representation of particles following a mathematical power-law size distribution with a global mean refractive index. Even though SIM-4 is frequently used in simulating the IOPs of particles [30,32], Fig. 2 illustrates that the actual particle assemblage in a natural environment can deviate significantly from this simplistic generalization.

2.4. Closure

IOPs follow the additive rule. For example, the total particulate scattering coefficient (b_p) can be expressed in the form:

$$b_p(\lambda) = \sum_{j=1}^{M} b_{p,j}(\lambda) \tag{2}$$

where j denotes different particle populations. If the size and refractive index distributions are known for a particle population, the corresponding scattering coefficient can be calculated:

$$(b_p)_j \int_{D_{\min}}^{D_{\max}} Q_b(\lambda, D, n_j) S_j(D) F_j(D) dD \tag{3}$$

where $Q_b(\lambda,D, n_j)$ is the dimensionless efficiency factor for scattering, which varies with the wavelength (λ), size (D), the complex refractive index n_j, and the shape of particles; S_j is the mean geometric cross-section area of particles; and $F_j(D)$ is the particle size distribution. Because FC derives the number concentration $N_{dj,nj}$ of particles of refractive index n_j in each size bin (D_j) based on the assumption that particles are spherical, Eq. (3) can be rewritten as:

$$(b_p)_j = \sum_{D_j n_j} Q_b(\lambda, D_j, n_j) \left(\frac{\pi D_j^2}{4}\right) N_{D_j, m_j} \tag{4}$$

To calculate the other IOPs of a_p, c_p, or β_p, we simply replaced the efficiency factor Q_b in Eq. (4) with the corresponding efficiency factor. The effect of particle shape and structure on achieving optical closure is implicitly included in computing the efficiency factors. In this study, we used three particle models to calculate the efficiency factors.

2.4.1. Homogeneous spherical model

The efficiency factors were calculated using the Lorenz-Mie theory by representing particles as homogeneous spheres. This is also the method used in Agagliate et al. [4]. Note that the estimation of particle size and refractive index from the FC method is based on the homogeneous spherical assumption [2].

2.4.2. Coated spherical model

A shell was added to the homogeneous sphere model to represent the cell membrane. The coated sphere model is capable of simulating the scattering and particularly the backscattering of phytoplankton cells reasonably well [19,22,24,27,28].

For the membrane, we followed Poulin et al. [27] for *T. pseudonana* and assumed a constant thickness of 0.1 µm and a constant refractive index of 1.1 with no absorption. The refractive index for the core (n_{r_core}) was estimated using the FC-derived refractive index (n_r) and the volume-fraction weighting:

$$\frac{V_{core}}{V} n_{r\_core} + \frac{V_{shell}}{V} n_{r\_shell} = n_r \tag{5}$$

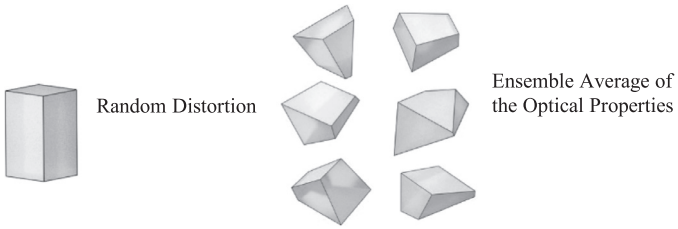

Fig. 3. An ensemble of non-symmetric hexahedra generated by randomly distorting a regular hexahedron. The optical properties averaged over the ensemble are regarded as the surrogates of oceanic particles.

where V is the volume of the particles, V_{core} and V_{shell} are the volumes for the core and shell, respectively, and n_{i_core} is set to 0.0015 [27] for all wavelengths.

For both homogeneous and coated spherical particle models, a Matlab code developed by Zhang [38] was used to calculate the efficiency factors based on the Lorenz-Mie scattering theory.

2.4.3. Non-symmetric hexahedron model

Fig. 3 illustrates examples of particles represented by the non-symmetric hexahedron model, which has been shown to reproduce the observed angular scattering by mineral aerosol particles well [6]. Improved techniques have been developed to compute the scattering by such hexahedra over the optically significant size range for oceanic particles [31,35].

In this study, the dataset of hexahedron scattering computed by Xu et al. [35] was used to generate the efficiency factors. The size parameter for a hexahedron is defined as the surface area equivalent diameter of a sphere.

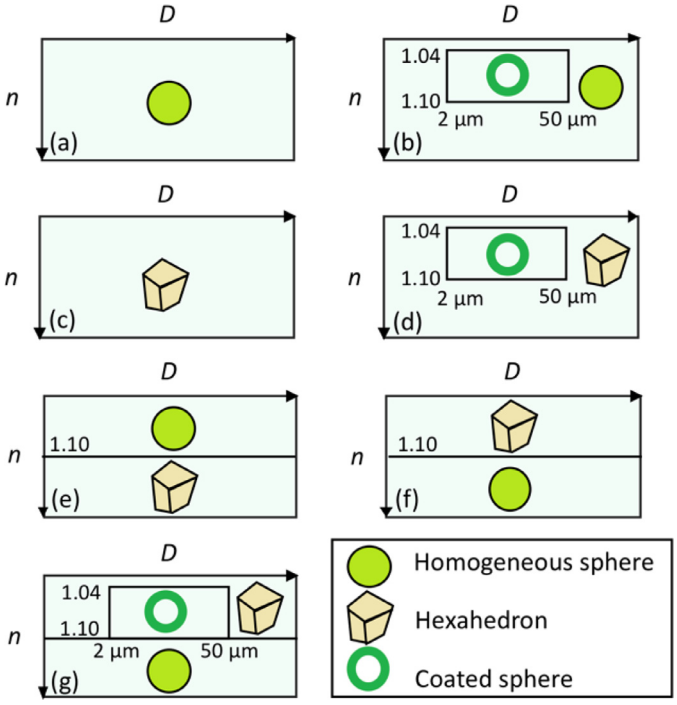

Fig. 4. Three particle shape and structure (PSS) models and seven combinations used in computing the single particle optical properties as a function of particle size (D) and refractive index (n). a) Homogeneous sphere; b) Coated sphere for phytoplankton grouping and homogeneous sphere for the rest; c) Hexahedron; d) Coated sphere for phytoplankton grouping and hexahedron for the rest; e) Homogeneous sphere for organic matter and hexahedron for inorganic matter; f) Hexahedron for organic matter and homogeneous sphere for inorganic matter; g) Hexahedron for organic matter, homogeneous sphere for inorganic matter, and coated sphere for phytoplankton grouping.

2.4.4. Forward modeling

To assess the effects of particle shape and structure on the closure, we used seven combinations of three particle models to reconstruct the bulk IOPs and to compare these results with in situ measurements (Fig. 4).

The effect of particle shape was examined in four cases: homogeneous spheres for all particles of all sizes (Fig. 4a), homogeneous hexahedra for all particles of all sizes (Fig. 4c), spheres for organic matter ($n_r < 1.1$) of all sizes and hexahedra for inorganic matter ($n_r > 1.1$) of all sizes (Fig. 4e), and spheres for inorganic matter of all sizes and hexahedra for organic matter of all sizes (Fig. 4f).

The effect of particle structure was examined mainly for phytoplankton particles, that we defined as having mean n_r from 1.04–1.10 [1] and sizes 2–50 µm. The phytoplankton particles are represented by coated spheres and the other particles in a sample are either spheres (Fig. 4b) or hexahedra (Fig. 4d). Coated spheres were not used for particles < 2 µm because of the difficulty of accurately modeling a very thin coating for very small particles. Note that the range of n_r for phytoplankton particles was based on FC-derived n_r, and the shell was assumed to have $n = 1.1$ without an imaginary part in applying the coated sphere model. The index for the core was estimated using Eq. (5). Finally, both effects of shape and structure are examined using a three-component model, representing phytoplankton particles using coated spheres, other organic matter represented by spheres, and inorganic matter using hexahedra (Fig. 4g). We refer to the seven particle shape and structure (PSS) models in Fig. 4a-g as PSS-a to -g, respectively.

Finally, for all seven particle models, we utilized each of the four PSD models (SIM-1, −2, −3, and −4) shown in Fig. 2 to investigate the effect of particle size and index distributions.

2.5. Closure evaluation

To evaluate closure, we used root mean square non-biased error (RMSNE):

$$RMSNE = \sqrt{\frac{1}{N}\sum_{i=1}^{N}\left[\frac{f_i - y_i}{\frac{f_i+y_i}{2}}\right]^2} \quad (6)$$

where f_i is the estimated value and y_i denotes the in situ IOP measurements.

3. Results

3.1. Overall closure

Fig. 5 shows the closure agreement between simulated and measured IOPs (a_p, b_p, c_p and $\beta_p(124)$) for different combinations of particle shapes and size distributions. Among the four particle size and index models, the most complex one that fully utilizes the FC measurements (SIM-1 in Fig. 2a, blue lines in Fig. 5), provided the best closure for all the three IOPs, regardless of the PSS model used. The uncertainty in simulating the IOPs increases as the complexity of the size and index distributions of natural particle assemblages is progressively simplified in using models SIM-1, SIM-2, SIM-3 and SIM-4. The average RMSNE values for the SIM-1 model were approximately 0.52 whereas those for the SIM-2, SIM-3 and SIM-4 models were approximately 0.56, 0.63 and 0.68, respectively. This suggests that (1) natural particles are indeed complex in size and composition; (2) this complexity is reflected in the IOPs; and therefore (3) it is important, whenever possible, to account for this

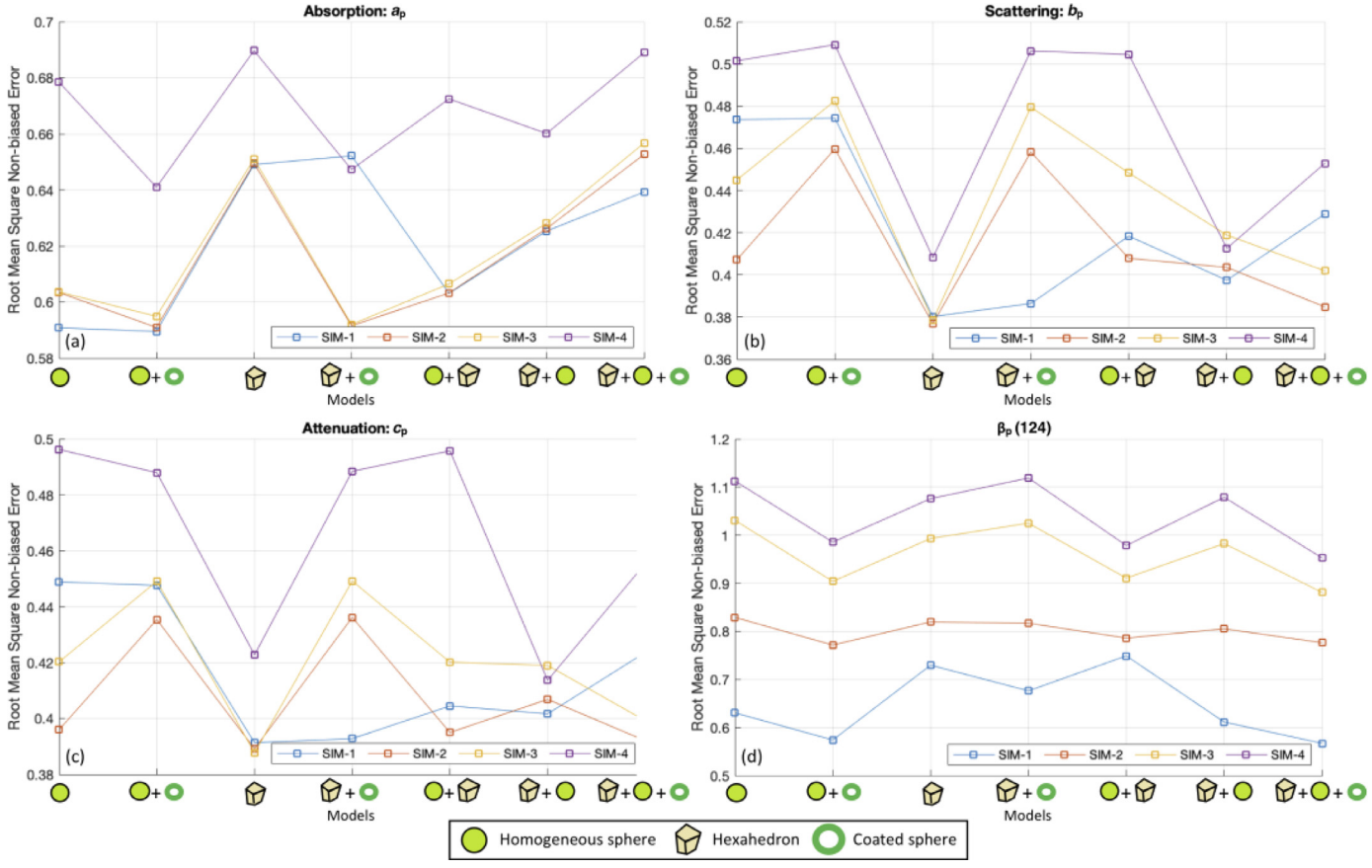

Fig. 5. RMSNEs between simulated and measured IOPs for particulate a) absorption, b) scattering, c) $\beta(124°)$ and d) attenuation. The x-axis represents different combinations of three models for particle shape (Fig. 4). The four colors correspond to the four SIM models for particle size distribution (Fig. 2) (For interpretation of the references to color in this figure legend, the reader is referred to the web version of this article.).

natural complexity in simulating the optical properties of the particles in the ocean. The SIM-1 model is similar to the model in Agagliate et al. [4]. Our RMSNE is slightly higher than theirs for scattering and backscattering, and absorption is better reproduced in our case. This might be due to the different imaginary parts of the refractive index that were used (~0.0012 vs 0.0001 or 0.0015 for FC measured particles and 0.0013 vs 0 for extrapolated particles).

While different SIM models performed similarly for all IOPs, different PSS models and their combinations performed differently for different IOPs. In the following, we examine the performance of different PSS models combined with the SIM-1 size and index model. For a_p (Fig. 5a), the best closure was for the PSS-a (spherical, RMSNE = 0.59) or the PSS-b (spherical + coated spherical, RMSNE = 0.59) models. For b_p (Fig, 5b), the PSS models with the least RMNSE for all SIM models were PSS-c (hexahedral, RMSNE = 0.38) and PSS-d (hexahedral and coated spheres, RMSNE = 0.39) models. For $\beta_p(124)$, four models, PSS-a (spheres, RMSNE = 0.63), PSS-b (spheres + coated spheres, RMSNE = 0.57), PSS-f (hexahedra + spheres, RMSNE = 0.61) and PSS-g (hexahedra + spheres + coated spheres, RMSNE = 0.57) performed similarly well (Fig. 5d). On the other hand, the PSS-c (hexahedral, RMSNE = 0.39) and the PSS-d (hexahedral + coated spherical, RMSNE = 0.39) models performed best for c_p closure (Fig. 5c).

Interestingly, the PSS models tend to perform oppositely between a_p and c_p (comparing Fig. 5a and c). For example, the hexahedral (PSS-a) and spherical and coated-spherical (PSS-b) models, which performed the best for a_p, performed worst for c_p.

The fact that no particular PSS model combination performed consistently better than the Lorenz-Mie theory (which assumes homogenous spheres) suggests that either the optical parameters are not especially sensitive to shape, or that our more complex PSS optical models are still insufficient to adequately represent or parameterize particle shape effects. The homogenous sphere is also expected to perform well because it is used to derive the FC size and refractive index distributions. It may also indicate that more information is necessary to provide the right inputs to the models (e.g. shell thickness and refractive index) for the observed population. For example, Poulin et al. [27] demonstrated that a variation of 0.03 in the shell's refractive index may cause an increase of ~50% of the calculated value of backscattering, so the results would be different with other inputs.

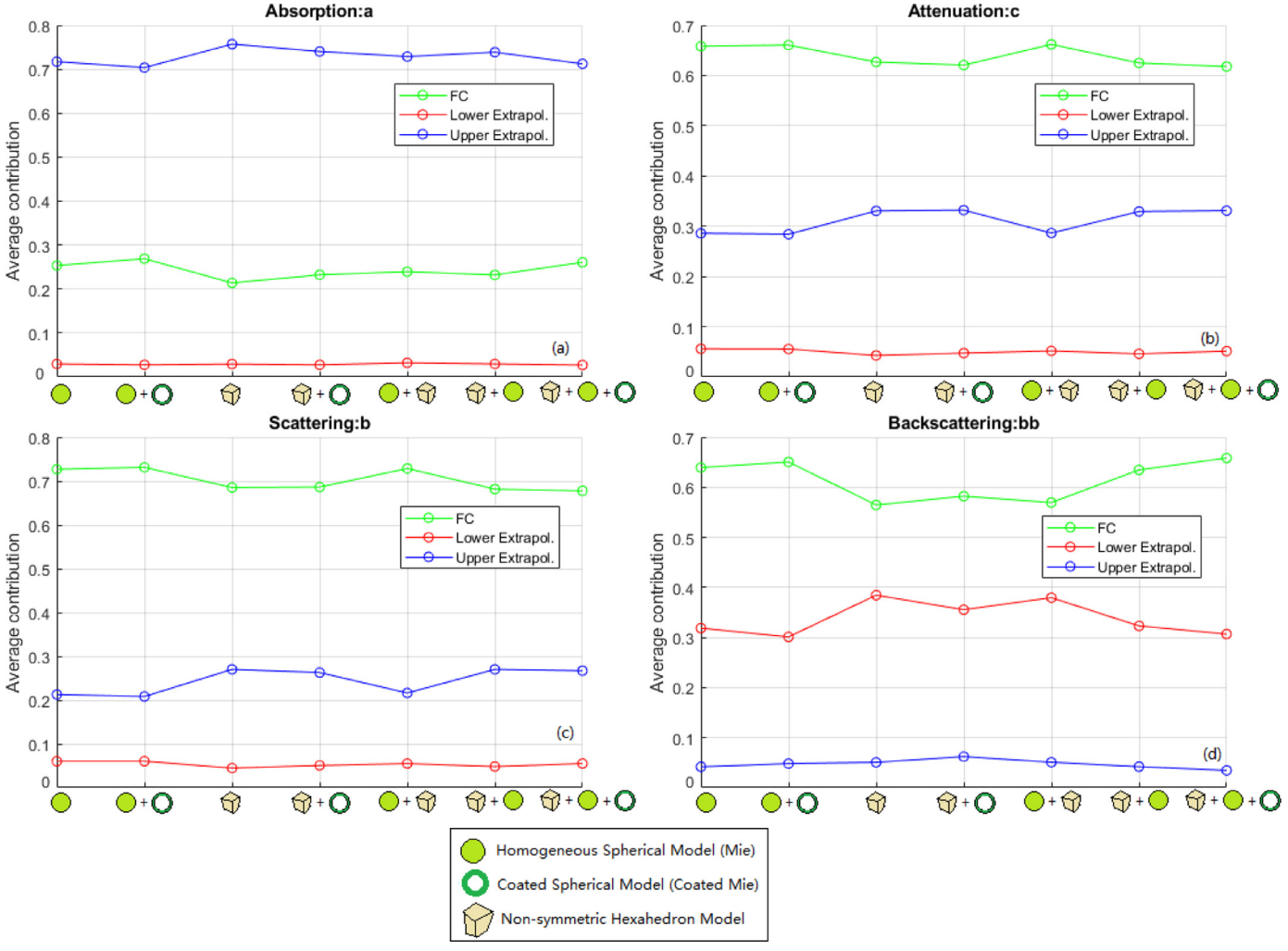

Fig. 6. Fractional contribution to a) absorption, b) attenuation, c) scattering and d) backscattering from the size range 0.5 – 20 μm detected by FC (green) and in extrapolated size ranges 0.5 μm (red) and size ranges > 20 μm (blue) (For interpretation of the references to color in this figure legend, the reader is referred to the web version of this article.).

3.2. Size-fractioned contribution

Fig. 6 compares the fractional contributions to each of the three IOPs from upper and lower extrapolations and FC-detected particles among the seven particle shape and structure models.

Particulate contributions to different IOPs did not show large variations between different PSS models. Particles of sizes $> 20\,\mu$m contributed to over 70% of absorption (Fig. 6a), and particles within the FC detectable range were responsible for approximately 20–30%. The lower extrapolation (smaller particles) contributed least, below 5% regardless of PSS models. For attenuation (Fig. 6b), FC detected particles contributed most, between 60% and 70%. Larger particles contributed around 30% of attenuation, and smaller particles only 5%. Similar to attenuation, the fractional contributions to scattering (Fig. 6c) were mainly due to FC-sized particles (~70%), and about 20–30% and <10% were due to smaller and larger particles, respectively. FC and smaller particles contributed to more than 90% of backscattering (Fig. 6d), among which about 60% were due to particles of sizes 0.5 – $20\,\mu$m and 30 – 40% due to smaller particles, whereas larger particles only contributed about 5%. Overall, particles of sizes $> 20\,\mu$m contributed the most to a_p while FC-detectable particles, of sizes 0.5 – $20\,\mu$m, largely contributed to c_p, b_p, and b_{bp}. These results agree with those of Agagliate et al. [4] for size-fractioned contributions.

4. Discussion

4.1. Cumulative contribution analysis

Stramski and Kiefer [30] simulated the cumulative contribution by oceanic particles of sizes that follow the Junge distribution with a slope of -4 and found that the maximum contribution to the backscattering coefficient is located at about 0.16 µm regardless of the refractive index, and the bulk of the backscattering effect was

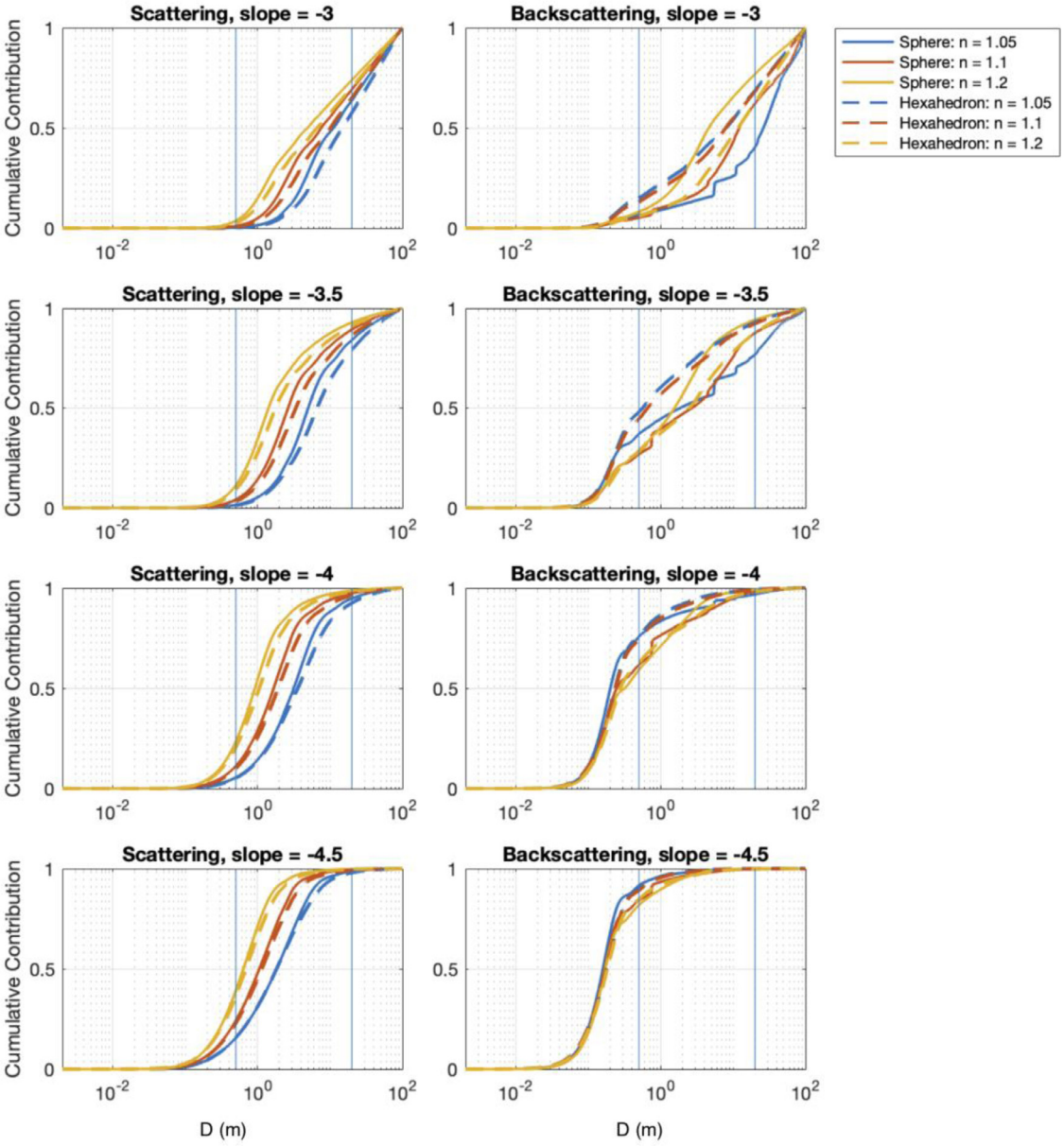

Fig. 7. Cumulative contribution to the total scattering and backscattering by particles of various sizes (D) following the Junge distribution with different slopes. For spheres, the size is the diameter and for hexahedra, the size is the surface area equivalent diameter. Solid lines are the results for spherical particles and dotted lines for hexahedral particles. Two vertical blue lines indicate FC detectable range of 0.5–$20\,\mu$m.

caused by particles of sizes < 0.33 µm. For total scattering, the major contribution was from particles of sizes between 1–5 μm, but varying with refractive index. On the other hand, our study shows that FC sized particles (0.5 – 20 µm) are important to both scattering and backscattering (Fig. 6c and d). To better understand this discrepancy, we expanded the work of Stramski and Kiefer by using both spherical and hexahedral shapes instead of using the spherical approximation, and we tested additional values besides −4 for the slope of Junge's distribution. The results are summarized in Fig. 7.

For scattering (Fig. 7, left side), as Junge's slope increased from −3 to −4.5, the contribution of particles smaller than 1 μm increased. Meanwhile, with a higher refractive index, smaller particles have a larger contribution to scattering. The average contribution of particles of sizes 0.5 – 20 μm is > 50% regardless of the slope values. This is consistent with our result shown in Fig. 6c. Also, particle shape has a minimal impact on the cumulative distribution of the total scattering.

For backscattering (Fig. 7, right side), the fractional contribution and the effect of particle shape varied with Junge's slope. When slope = −3, particles smaller than 0.5 μm only contributed to less than 10% of backscattering. As the refractive index increased, the contribution of FC-detected particles increased too, for the spherical model. Especially when $n = 1.2$, the contribution of particles between 0.5 to 20 μm to backscattering is more than 50%. When Junge's slope became steeper, the contribution of smaller particles increased. When the slope equaled −4.5, most of the contribution to backscattering came from particles smaller than 0.5 μm, and the contribution was independent of the refractive index. In our study, the slopes of 50 samples ranged from −2.5 to −3.5, which means FC-detected particles contribute most to backscattering, and also explains why the extrapolated particles of sizes < 0.5 μm contributed to 30–40% of the total backscattering in Fig. 6d. The fact that our measured Junge slopes were in the range of −2.5–3.5 can also explain in part that we found less contribution from particles of sizes < 0.5 μm than Stramski and Kiefer [30], who found that particles smaller than 1 µm contributed the most to the backscattering coefficient with a Junge slope of −4. They also used the Junge slope for the whole PSD and assumed a single refractive index for the whole population, which might bring their results further from ours. The effect of particle shape is more significant when slope is −3.5 or lower and negligible when the slope is −4 or steeper.

The FC approach estimates sizes and refractive indices of particles from FC measurements of forward and side scatter and is based on the assumption that these optical properties can be interpreted using the Lorenz-Mie theory with homogeneous spheres. Consequently, when FC-derived PSDs and refractive indices are used to estimate bulk IOPs that are also calculated using the Lorenz-Mie theory, there is a level of internal self-consistency that might be expected to contribute to the spherical particle model performing as well as other PSS models (Fig. 5). The spherical model did indeed give good results with a and $\beta(124)$ and average results for b and c. A degree of caution is required in interpretation of these results, as there is a level of circularity in using FC-derived PSDs and PRIDs to test the applicability of the Lorenz-Mie theory to represent IOPs in natural waters.

For size and refractive index distribution models, the simplest SIM model using a single Junge distribution and refractive index clearly leads to the worst results for all IOPs, suggesting that it underestimates the complexity of size distributions and refractive indices of natural particles. Other more complex SIM models performed similarly for a, b, and c, but for $\beta(124)$, the most complex model using measured PSDs and PRIDs performed better than all other models. This indicates that backscattering may be more sensitive to both particle numbers and refractive indices and that, where possible, the complexity of natural particle assemblages including size and refractive index diversity should be taken into account when modeling IOPs.

4.2. Sources of uncertainty

Great care was taken to ensure the reliability of IOP measurements. As stated before, and shown in Fig. 1, an iterative method was used to correct absorption, attenuation and volume scattering function at 124°. However, some potential sources of errors may explain at least in part the differences between our IOP measurements and models. For instance, the fact that the refractive index was measured at 488 nm while closure was evaluated at 532 nm and that we used imaginary parts of the refractive index from the literature also potentially affect the results, particularly for absorption. In addition, even with the more complex combinations of coated spherical and hexahedral models, the modeled shapes were most likely different from the realistic shapes of the measured oceanic particles. Cell size is also difficult to evaluate with non-spherical particles. We used surface area equivalent diameter for hexahedral models, but a different equivalent diameter could potentially be more representative of our measured particles' size. Moreover, the use of single theoretical values of coating thickness and refractive index is also likely to differ from reality. It is necessary for instrumentation to be improved to provide detailed information on particle shape and structure that allow parameterization of more sophisticated PSS models. Considering the current lack of information on these factors, we consider that our assumptions are reasonable first-order approximations.

Conclusion

Overall, this study shows that more complex SIM models, taking into account FC-derived refractive indexes and particle size distributions, give better results than the simpler models using a single refractive index and/or a specific Junge slope. Although it was not possible to identify a single outstanding PSS model, it is a reasonable hypothesis that particle shape and structure significantly contribute to residual discrepancies between measured and modelled bulk IOPs [10,15,24,34]. In addition, small particles contributed in smaller proportions to IOPs, particularly in backscattering, than previously predicted by Stramski and Kiefer [30] assuming a particle size distribution of a Junge slope of −4. This is mainly because observed particle size distributions had lower effective Junge slopes (mean = −3.36), meaning a relatively high abundance of larger particles and consequently greater contributions to IOPs from larger size classes.

Funding

The HE442 cruise with RV Heincke was conducted under grant number AWI-HE442 to R. Röttgers, HZG. Agagliate received funding from the MASTS pooling initiative (The Marine Alliance for Science and Technology for Scotland). MASTS is funded by the Scottish Funding Council (grant reference HR09011) and contributing institutions. PY acknowledges support by the endowment funds related to the David Bullock Harris Chair in Geosciences at Texas A&M University,grant number 02-512231-00001. YZ, LH, CP and XZ acknowledge support by NASA (NNX13AN72G, NNX15AC85G, 80NSSC18M0024, 80NSSC17K0656) and NSF (1917337).

Declaration of Competing Interest

None.

Acknowledgements

The authors further wish to thank the captain and the crew of RV Heincke for their support and help during the HE442 research cruise, and Dr Rüdiger Röttgers (HZG, Germany) for supporting our participation on the cruise. We also thank an anonymous reviewer for their comments to improve this work.

References

[1] Aas E. Refractive index of phytoplankton derived from its metabolite composition. J Plankton Res 1996;18(12):2223–49.
[2] Ackleson SG, Spinrad RW. Size and refractive index of individual marine particulates: a flow cytometric approach. Appl Opt 1988;27(7):1270–7.
[3] Agagliate J, Röttgers R, Twardowski MS, McKee D. Evaluation of a flow cytometry method to determine size and real refractive index distributions in natural marine particle populations. Appl Opt 2018;57(7):1705–16.
[4] Agagliate J, Lefering I, McKee D. Forward modeling of inherent optical properties from flow cytometry estimates of particle size and refractive index. Appl Opt 2018;57(8):1777–88.
[5] Babin M, Morel A, Fournier-Sicre V, Fell F, Stramski D. Light scattering properties of marine particles in coastal and open ocean waters as related to the particle mass concentration. Limnol Oceanogr 2003;48(2):843–59.
[6] Bi L, Yang P, Kattawar GW, Kahn R. Modeling optical properties of mineral aerosol particles by using nonsymmetric hexahedra. Appl Opt 2010;49(3):334–42.
[7] Chang G, Barnard A, Zaneveld JRV. Optical closure in a complex coastal environment: particle effects. Appl Opt 2007;46(31):7679–92.
[8] Chang G, Whitmire AL. Effects of bulk particle characteristics on backscattering and optical closure. Opt Express 2009;17(4):2132–42.
[9] p. 1-38 Clavano WR, Boss E, Karp-Boss L. Inherent optical properties of non–spherical marine-like particles - from theory to observation. Oceanography and marine biology: an annual review. Gibson RN, Atkinson RJA, Gordon JDM, editors Taylor & Francis; 2007.
[10] Dall'Olmo G, Westberry TK, Behrenfeld MJ, Boss E, Slade WH. Significant contribution of large particles to optical backscattering in the open ocean. Biogeosciences 2009;6(6):947.
[11] Davies EJ, McKee D, Bowers D, Graham GW, Nimmo-Smith WAM. Optically significant particle sizes in seawater. Appl Opt 2014;53(6):1067–74.
[12] Duforêt-Gaurier L, Moutier W, Guiselin N, Thyssen M, Dubelaar G, Mériaux X, et al. Determination of backscattering cross section of individual particles from cytometric measurements: a new methodology. Opt Express 2015;23(24):31510–33.
[13] Fournier GR, Forand JL. Analytic phase function for ocean water. In Ocean Optics XII 1994;2258(October):194–201 International Society for Optics and Photonics.
[14] Green RE, Sosik HM, Olson RJ, DuRand MD. Flow cytometric determination of size and complex refractive index for marine particles: comparison with independent and bulk estimates. Appl Opt 2003;42(3):526–41.
[15] Harmel T, Hieronymi M, Slade W, Röttgers R, Roullier F, Chami M. Laboratory experiments for inter-comparison of three volume scattering meters to measure angular scattering properties of hydrosols. Opt Express 2016;24(2):A234–56.
[16] Jonasz M, Fournier G. Light scattering by particles in water. Elsevier; 2007.
[17] Junge CE. Air chemistry and radioactivity. Academic Press; 1963. p. 382–3.
[18] Kirk JT, Oliver RL. Optical closure in an ultraturbid lake. J Geophys Res Ocean 1995;100(C7):13221–5.
[19] Kitchen JC, Zaneveld JRV. A three-layered sphere model of the optical properties of phytoplankton. Limnol Oceanogr 1992;37(8):1680–90.
[20] Lefering I, Bengil F, Trees C, Röttgers R, Bowers D, Nimmo-Smith A, et al. Optical closure in marine waters from in situ inherent optical property measurements. Opt Express 2016;24(13):14036–52.
[21] McKee D, Piskozub J, Röttgers R, Reynolds RA. Evaluation and improvement of an iterative scattering correction scheme for in situ absorption and attenuation measurements. J Atmos Ocean Technol 2013;30(7):1527–41.
[22] Meyer RA. Light scattering from biological cells: dependence of backscatter radiation on membrane thickness and refractive index. Appl Opt 1979;18(5):585–8.
[23] Moutier W, Duforêt-Gaurier L, Thyssen M, Loisel H, Mériaux X, Courcot L, et al. Scattering of individual particles from cytometry: tests on phytoplankton cultures. Opt Express 2016;24(21):24188–212.
[24] Organelli E, Dall'Olmo G, Brewin RJ, Tarran GA, Boss E, Bricaud A. The open-ocean missing backscattering is in the structural complexity of particles. Nat Commun 2018;9(1):5439.
[25] Pegau WS, Gray D, Zaneveld JRV. Absorption and attenuation of visible and near-infrared light in water: dependence on temperature and salinity. Appl Opt 1997;36(24):6035–46.
[26] Pegau WS, Zaneveld JRV, Voss KJ. Toward closure of the inherent optical properties of natural waters. J Geophys Res Ocean 1995;100(C7):13193–9.
[27] Poulin C, Zhang X, Yang P, Huot Y. Diel variations of the attenuation, backscattering and absorption coefficients of four phytoplankton species and comparison with spherical, coated spherical and hexahedral particle optical models. J Quant Spectrosc Radiat Transf 2018;217:288–304.
[28] Quirantes A, Bernard S. Light scattering by marine algae: two-layer spherical and nonspherical models. J Quant Spectrosc Radiat Transf 2004;89(1–4):311–21.
[29] Stramski D, Boss E, Bogucki D, Voss KJ. The role of seawater constituents in light backscattering in the ocean. Prog Oceanogr 2004;61(1):27–56.
[30] Stramski D, Kiefer DA. Light scattering by microorganisms in the open ocean. Prog Oceanogr 1991;28(4):343–83.
[31] Sun B, Yang P, Kattawar GW, Zhang X. Physical-geometric optics method for large size faceted particles. Opt Express 2017;25(20):24044–60.
[32] Twardowski MS, Boss E, Macdonald JB, Pegau WS, Barnard AH, Zaneveld JRV. A model for estimating bulk refractive index from the optical backscattering ratio and the implications for understanding particle composition in case I and case II waters. J Geophys Res Ocean 2001;106(C7):14129–42.
[33] Tzortziou M, Herman JR, Gallegos CL, Neale PJ, Subramaniam A, Harding LW Jr, et al. Bio-optics of the Chesapeake Bay from measurements and radiative transfer closure. Estuar Coast Shelf Sci 2006;68(1–2):348–62.
[34] Whitmire AL, Pegau WS, Karp-Boss L, Boss E, Cowles TJ. Spectral backscattering properties of marine phytoplankton cultures. Opt Express 2010;18(14):15073–93.
[35] Xu G, Sun B, Brooks SD, Yang P, Kattawar GW, Zhang X. Modeling the inherent optical properties of aquatic particles using an irregular hexahedral ensemble. J Quant Spectrosc Radiat Transf 2017;191:30–9.
[36] Zhang X, Hu L, He MX. Scattering by pure seawater: effect of salinity. Opt Express 2009;17(7):5698–710.
[37] Zhang X, Lewis M, Johnson B. Influence of bubbles on scattering of light in the ocean. Appl Opt 1998;37(27):6525–36.
[38] Zhang X. ZhangMie [Matlab function] 2018. http://und.edu/faculty/zhang-xiaodong/_files/docs/programs/zhangmie.m.